Journal of Materials Chemistry A

PAPER

View Article Online
View Journal | View Issue

Cite this: *J. Mater. Chem. A*, 2018, **6**, 4179

High-efficiency bulk heterojunction perovskite solar cell fabricated by one-step solution process using single solvent: synthesis and characterization of material and film formation mechanism†

Chun-Yu Chang,‡[a] Chieh-Ping Wang,‡[a] Rathinam Raja,[b] Leeyih Wang,[b] Cheng-Si Tsao[ac] and Wei-Fang Su *[a]

Received 9th September 2017
Accepted 30th January 2018

DOI: 10.1039/c7ta07939g

rsc.li/materials-a

Bulk heterojunction (BHJ) perovskite solar cells have recently attracted increased interest because of a significantly enhanced interface between perovskite and the n-type material in the active layer for efficient charge separation and increased power conversion efficiency (PCE). [6,6]-Phenyl-C_{61}-butyric acid methyl ester ($PC_{61}BM$) is the most commonly used n-type material in BHJ perovskite solar cells owing to its high electron mobility. However, it is very difficult to fabricate BHJ perovskite films because of the poor solubility of $PC_{61}BM$ in the commonly used solvent dimethylformamide (DMF). In this study, we introduced two kinds of fluorinated $PC_{61}BM$ (3F-$PC_{61}BM$ and 5F-$PC_{61}BM$) as n-type materials in a BHJ perovskite film, which have higher solubility in DMF than that of $PC_{61}BM$. Thus, a BHJ perovskite film can be easily fabricated in one step using a single solvent in a BHJ precursor solution system for planar perovskite solar cells. A BHJ device with a high PCE of 16.17% can be obtained by adding 0.1 wt% of 3F-$PC_{61}BM$ in a perovskite precursor solution to fabricate a solar cell, which outperforms the PCE of 14.12% of the pristine device. However, the addition of 5F-$PC_{61}BM$ decreased the PCE to lower than that of the pristine device regardless of its amount. We systematically studied the effects of the amount and type of fluorinated $PC_{61}BM$ on the morphology of BHJ perovskite films using SEM, AFM, GISAXS and GIWAXS. The results reveal that 3F-$PC_{61}BM$ can fill the pinholes between perovskite grains and passivate the defects in the pristine film. Thus, the current density (J_{sc}) is greatly increased. On the other hand, the self-aggregation of 5F-$PC_{61}BM$ in BHJ perovskite films caused the films to be full of large voids, which led to poor device performance. The dense and flat surface morphology of BHJ perovskite films containing 3F-$PC_{61}BM$ can also prevent the permeation of moisture into grain boundaries and enhance the device stability. Therefore, the device could maintain 80% of its original efficiency over 550 hours without any encapsulation in comparison with 240 hours for the pristine device. Our results provide a novel strategy for fabricating high-PCE and high-stability BHJ perovskite solar cells for the production of low-cost solar cells in the near future.

Introduction

Recently, organic–inorganic metal halide perovskites have become promising materials in solar cell research owing to their properties of long carrier diffusion length[1–6] and a high absorption coefficient.[7–10] Currently, the highest certified power conversion efficiency (PCE) of a perovskite-based solar cell is 22.1%.[11] There are three main kinds of device structures, namely, perovskite-sensitized devices,[8,12–14] meso-superstructured devices[15–17] and planar heterojunction (PHJ) devices.[18–22] In comparison with the other two kinds of device, PHJ devices have been extensively investigated because the whole device can be fabricated at a low temperature of 150 °C.[18,20,22] Many studies of PHJ solar cells report that a uniform perovskite film composed of large crystal grains is closely related to a high PCE. Recently, the bulk heterojunction (BHJ) structure of a fullerene derivative: perovskite blend film as the light-absorbing active layer has attracted increased interest because of significantly enhanced photovoltaic performance.[23–28] This BHJ structure is fabricated by the blending of perovskite with an appropriate amount of fullerene derivatives. The BHJ structure increases the interface between perovskite and the fullerene derivative to form a network

[a]*Department of Materials Science and Engineering, National Taiwan University, Taipei 10617, Taiwan. E-mail: suwf@ntu.edu.tw*

[b]*Center of Condensed Matter Science, National Taiwan University, Taipei 10617, Taiwan*

[c]*Institute of Nuclear Energy Research, Taoyuan 32546, Taiwan*

† Electronic supplementary information (ESI) available. See DOI: 10.1039/c7ta07939g

‡ These authors contributed equally to this work.

structure for the efficient generation and transportation of charge carriers, which results in increased PCE.

Sargent *et al.* first introduced [6,6]-phenyl-C_{61}-butyric acid methyl ester ($PC_{61}BM$) into a perovskite solar cell to fabricate a BHJ device. Owing to the poor solubility of $PC_{61}BM$ in dimethylformamide (DMF), which is the solvent commonly used for dissolving the perovskite precursor, they used a co-solvent process to solve this problem. They separately dissolved $PC_{61}BM$ in chlorobenzene and the perovskite precursor in DMF. Then, the two solutions were mixed by a high shear force to forcibly disperse $PC_{61}BM$ in the perovskite precursor. They showed that BHJ devices made by this method can display significantly reduced hysteresis behavior and increase the PCE from 12.0% to 14.4%.[23] However, chlorobenzene is a poor solvent for perovskite,[29] and a homogeneous co-solvent system is difficult to obtain by simply mixing two solutions of $PC_{61}BM$ in chlorobenzene and the perovskite precursor in DMF. Wu *et al.* adopted a two-step process to fabricate a BHJ perovskite film.[24] They initially deposited a mixed solution of lead iodide and $PC_{71}BM$ in DMF onto a substrate to form a blending film (PbI_2:$PC_{71}BM$), followed by a second deposition of methylammonium iodide (MAI) in isopropyl alcohol to finish the transformation of perovskite. $PC_{71}BM$ molecules can fill the perovskite grain boundaries and passivate the pinholes in the film by this method. However, $PC_{71}BM$ may hinder the diffusion of MAI to the bottom of the PbI_2:$PC_{71}BM$ film. The transformation of underlying PbI_2 grains into perovskite would be restricted. The incomplete transformation of the active layer may limit the photovoltaic performance. In addition, $PC_{71}BM$ is much more expensive than $PC_{61}BM$.

In order to increase the solubility of the fullerene derivative in the perovskite precursor solution or enhance the stability of the BHJ device, some research groups have tried to modify the fullerene to achieve these goals. Hsu *et al.* utilized cross-linkable $PC_{61}BM$ ([6,6]-phenyl-C_{61}-butyric styryl dendron ester, C-PCBSD) to increase the current density and stability of a BHJ device. They thermally annealed the BHJ perovskite film at 100 °C for two to six hours for the simultaneous transformation of perovskite and formation of cross-linked C-PCBSD.[25] However, a long annealing time may not only cause serious degradation of the perovskite film but also waste energy. Recently, Jen *et al.* incorporated a fluorine-modified fullerene derivative (DF-C_{60}) into a BHJ film. The low surface energy of the perfluorooctyl groups in DF-C_{60} caused this molecule to be preferentially distributed near the surface region of the BHJ film. The hydrophobic surface of DF-C_{60} can prevent the permeation of moisture into the film, and thus the stability of the perovskite solar cell is improved.[26] However, the long fluorinated carbon chains limit the solubility of DF-C_{60} in DMF. They also needed to use a co-solvent process to fabricate the BHJ perovskite film, as mentioned above. In summary, the tailoring of a BHJ perovskite solar cell by the addition of a fullerene derivative can be an effective way to increase the performance of a solar cell. However, most studies have adopted a co-solvent system[23,26,28] or another complex process,[24,25,27] in which it is difficult to control the quality of the BHJ perovskite film. In addition, no literature report has discussed the detailed characteristics and formation mechanisms of a BHJ fullerene derivative: perovskite film. A mechanistic understanding of how fullerene derivative molecules influence the morphology and crystallization of the perovskite phase with respect to the device performance is imperative but remains elusive at present.

In this study, we show a novel strategy for significantly increasing the PCE and long-term stability of BHJ perovskite solar cells by using semi-fluorinated $PC_{61}BM$. Trifluoroethyl or pentafluoropropyl groups were used to replace the methyl group on the side chain of $PC_{61}BM$ to form 3F-$PC_{61}BM$ and 5F-$PC_{61}BM$. *Via* modification by fluorination, the solubility of $PC_{61}BM$ in the perovskite precursor was improved significantly. Instead of a complex fabrication process such as a co-solvent or two-step process, we successfully fabricated a fluorinated $PC_{61}BM$: perovskite BHJ perovskite solar cell by a one-step single-solvent process. We systematically studied the effects of the amount and type of fluorinated $PC_{61}BM$ on the morphology of BHJ perovskite films using scanning electron microscopy (SEM), atomic force microscopy (AFM), and grazing-incidence small- and wide-angle X-ray scattering (GISAXS and GIWAXS). The formation mechanism of the perovskite film containing fluorinated $PC_{61}BM$ was elucidated. The correlation between the film morphology and device performance was clearly resolved.

Experimental

Materials and sample preparation

Methylammonium iodide (MAI) was synthesized according to the literature.[22] Lead(II) acetate trihydrate ($Pb(Ac)_2{\cdot}3H_2O$, 99.999%, Aldrich) was dehydrated at 80 °C in a vacuum oven for 3 hours before use. The pristine perovskite precursor solution was prepared by mixing MAI and dehydrated $Pb(Ac)_2$ in a molar ratio of 3 : 1 in anhydrous *N*,*N*-dimethylformamide (DMF, 99.8%, Sigma-Aldrich). The solution concentration was 40 wt%. For the BHJ precursor solution, the appropriate amount (from 0.1 wt% to 0.5 wt%) of 3F-$PC_{61}BM$ or 5F-$PC_{61}BM$ was directly incorporated into the perovskite precursor solution. All the precursor solutions were filtered through a 0.2 μm PTFE filter before a further spin-coating process.

The synthetic routes used for 3F-$PC_{61}BM$ and 5F-$PC_{61}BM$ were as follows. [6,6]-Phenyl-C_{61}-butyric acid (PCBA) was obtained from PCBM by treatment with hydrochloric acid and acetic acid in chlorobenzene under reflux for 12 h.[30] A mixture of PCBA (200 mg, 0.22 mmol) and 2,2,2-trifluoroethanol (44 mg, 0.44 mmol) was dissolved in 1,2-dichlorobenzene (100 mL) and ultrasonicated for 2 h and then cooled to 0 °C. Afterward, dimethylaminopyridine (DMAP) and dicyclohexylcarbodiimide (DCC) were added under an N_2 atmosphere. The reaction mixture was stirred under N_2 at 0 °C for 30 min and then at room temperature for 24 h. The solvents were removed in a high vacuum, and the residue was precipitated with methanol. The crude product was purified by column chromatography using toluene/hexane (25 : 75) as the eluent to afford 3F-$PC_{61}BM$ in 67% yield. ^{1}H NMR spectrum of 3F-$PC_{61}BM$ (400 MHz, $CDCl_3$, δ, ppm): 7.91–7.89 (m, 2H), 7.55–7.50 (m, 2H), 7.48–7.43 (m, 1H), 4.45 (q, 2H, J = 8.4 Hz), 2.92–2.88 (m, 2H), 2.61 (t, 2H, J = 7.6

Hz), 2.23–2.15 (m, 2H). ^{19}F NMR (376.5 MHz, $CDCl_3$, δ, ppm): −73.59 (t, J = 8.65 Hz, 3F). ^{13}C NMR (100 MHz, $CDCl_3$, δ, ppm): 171.3, 148.7, 147.6, 145.8, 145.2, 145.1, 145.0, 144.7, 144.6, 144.5, 144.4, 143.9, 143.7, 143.1, 143.0, 142.9, 142.9, 142.2, 142.1, 142.1, 140.9, 140.7, 138.0, 137.5, 136.5, 132.0, 128.5, 128.3, 124.2, 121.5, 79.7, 60.3 (q, J = 36.3 Hz), 51.6, 33.5, 33.3, 22.0. MALDI-TOF-MS m/z: calculated for $C_{73}H_{13}O_2F_3$ 978.09, found 977.96 (M^+).

The synthetic procedure of 5F-$PC_{61}BM$ was similar to that of 3F-$PC_{61}BM$. The reaction of PCBA (200 mg, 0.22 mmol) and 2,2,3,3,3-pentafluoro-1-propanol (67 mg, 0.44 mmol) afforded 5F-$PC_{61}BM$ in 59% yield. ^{1}H NMR spectrum of 5F-$PC_{61}BM$ (400 MHz, $CDCl_3$, δ, ppm): 7.91–7.88 (m, 2H), 7.55–7.51 (m, 2H), 7.48–7.44 (m, 1H), 4.56–4.49 (m, 2H), 2.92–2.88 (m, 2H), 2.60 (t, 2H, J = 7.6 Hz), 2.23–2.15 (m, 2H). ^{19}F NMR (376.5 MHz, $CDCl_3$, δ, ppm): −83.72, −123.33. ^{13}C NMR (100 MHz, $CDCl_3$, δ, ppm): 171.3, 148.7, 147.6, 145.8, 145.2, 145.0, 144.8, 144.7, 144.6, 144.5, 144.4, 144.0, 143.7, 143.1, 143.0, 142.9, 142.9, 142.2, 142.1, 142.1, 141.0, 140.7, 138.0, 137.5, 136.5, 132.0, 128.5, 128.3, 79.7, 59.1 (t, J = 27.4 Hz), 51.6, 33.5, 33.4, 22.0. MALDI-TOF-MS m/z: calculated for $C_{74}H_{13}O_2F_5$ 1028.08, found 1028.08 (M^+).

Fabrication of the perovskite solar cells

Our BHJ perovskite solar cells had the structure of ITO/PEDOT:PSS/fluorinated $PC_{61}BM$: perovskite/$PC_{61}BM$/PEI/Au. The fabrication procedure was as follows. Firstly, the ITO substrate (Buwon, 10 Ω) was cleaned sequentially with ammonia/hydrogen peroxide/deionized water, methanol, and isopropanol and treated with oxygen plasma for 15 minutes. Next, PEDOT:PSS was spin-coated on the as-cleaned ITO substrate at 3000 rpm for 30 seconds followed by baking at 140 °C for 20 minutes to form the hole transport layer. The ITO/PEDOT:PSS substrates were then transferred into a glove box under a nitrogen atmosphere, and the as-prepared precursor solutions were spin-coated at 2000 rpm for 40 seconds. The films were subsequently thermally annealed at 100 °C for 3 minutes to form the photoactive layer. Afterwards, the $PC_{61}BM$ solution (20 mg in 1 mL chlorobenzene) was spin-coated over the photoactive layer at 1000 rpm for 30 seconds to serve as the electron transport layer. Finally, a PEI interface-modifying layer and a gold electrode with a thickness of 100 nm were deposited on the top of the device to finish the fabrication of BHJ perovskite solar cells.

Characterization

For the characterization of photoelectronic performance, the devices were exposed under an AM 1.5G solar simulator (Newport 69920) with an irradiation intensity of 100 mW cm^{-2}, and the J–V curves were recorded using a voltage source meter (Keithley 2410). The PL spectra were recorded with a continuous-wave diode laser source (PDLH-440-25, DongWoo Optron Co. Ltd.), and the emission spectra were recorded with a photomultiplier tube detector system (PDS-1, DongWoo Optron Co. Ltd.). The TRPL spectra were recorded using a time-correlated single photon counting spectrometer (WELLS-001 FX, DongWoo Optron Co. Ltd.). The pulse laser had a wavelength of 440 nm and an average power of 1 mW and was operated with an excitation duration of 2 μs. The surface morphologies of the BHJ films were observed with a field emission SEM (JSM-6700F, JEOL) at an accelerating voltage of 10 kV. The surface height information was obtained by AFM (OMV-NTSC, Bruker). Simultaneous synchrotron GISAXS/GIWAXS measurements were performed at the 23A beamline of the National Synchrotron Radiation Research Center (NSRRC), Taiwan. The pristine and BHJ perovskite film were spin-coated on Si/PEDOT:PSS substrates. A monochromated X-ray beam with a wavelength of 1.24 Å and an incidence angle of 0.2° was employed to characterize the films. The sample-to-detector distances in the GISAXS and GIWAXS measurements were 461.1 cm and 14.3 cm, respectively. The 1D GISAXS profiles were obtained by linear integration of the 2D GISAXS patterns along the in-plane direction. Water contact angle measurements were performed using a contact angle goniometer (100SB, Sindatek Instrument Co. Ltd.).

Results and discussion

We adopted the p–i–n device structure of ITO/PEDOT:PSS/fluorinated $PC_{61}BM$: perovskite/$PC_{61}BM$/PEI/Au to fabricate the BHJ perovskite solar cells. Two strategies of material synthesis were employed to obtain high-quality BHJ perovskite films. The first strategy used lead acetate ($Pb(Ac)_2$) as the lead source for the perovskite.[31] The transformation process of $Pb(Ac)_2$ and MAI into perovskite is described as follows:

$$Pb(Ac)_2 + 3CH_3NH_3I \rightarrow CH_3NH_3PbI_3 + 2CH_3NH_3(Ac)\uparrow (Ac = CH_3COO)$$

Note that the by-product $CH_3NH_3(Ac)$ is thermally unstable and is easily evaporated during the thermal annealing process. This forces the reaction toward the right and accelerates the formation of perovskite. The use of lead acetate and MAI as the perovskite precursor materials can simplify the fabrication process of the BHJ film at 100 °C for only 5 minutes. The second strategy used fluorinated $PC_{61}BM$ as the n-type material in the BHJ perovskite film. Fig. 1(a) and (b) show the molecular

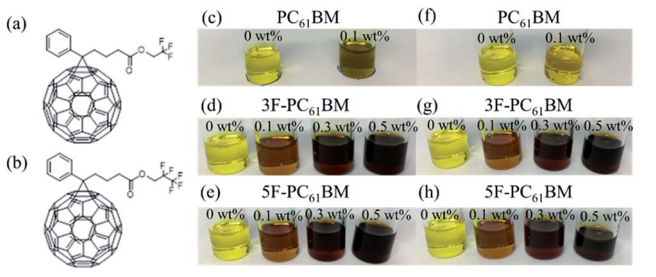

Fig. 1 Chemical structures of (a) 3F-$PC_{61}BM$ and (b) 5F-$PC_{61}BM$. Photos of BHJ perovskite precursor solutions containing different concentrations of $PC_{61}BM$, 3F-$PC_{61}BM$, and 5F-$PC_{61}BM$: (c)-(e) without filtration and (f)–(h) with filtration.

structures of 3F-$PC_{61}BM$ and 5F-$PC_{61}BM$, respectively, in which the methyl group on the side chain of $PC_{61}BM$ is replaced by fluoroalkyl chains with different lengths. 3F-$PC_{61}BM$ and 5F-$PC_{61}BM$ were synthesized *via* the esterification of [6,6]-phenyl-C_{61}-butyric acid (PCBA) by 2,2,2-trifluoroethanol and 2,2,3,3,3-pentafluoro-1-propanol, respectively, as shown in Scheme 1. The chemical structures of the synthesized compounds were confirmed by ^{1}H NMR, ^{13}C NMR, ^{19}F NMR and mass spectroscopy (see details in the Experimental section). The fluoroalkyl groups increased the molecular polarity and improved the solubility in DMF. The measured solubilities of 3F-$PC_{61}BM$ and 5F-$PC_{61}BM$ in DMF were 4.0 mg mL^{-1} and 2.5 mg mL^{-1}, respectively, which were twenty and twelve times higher, respectively, than that of $PC_{61}BM$ (0.2 mg mL^{-1}). It is worth noting that the low molecular polarity of the pentafluoropropyl group would make the solubility of 5F-$PC_{61}BM$ in DMF lower than that of 3F-$PC_{61}BM$. Nevertheless, we could still blend fluorinated $PC_{61}BM$, lead acetate and MAI in DMF as the precursor solution to fabricate the BHJ light-absorbing active layer by a one-step single-solvent process.

Before proceeding to fabricate the BHJ perovskite solar cells, we needed to carefully characterize the optical and electronic properties of 3F-$PC_{61}BM$ and 5F-$PC_{61}BM$ to ensure that they were suitable materials for the BHJ perovskite films. The space-charge-limited current (SCLC) model was adopted to calculate the electron mobilities of $PC_{61}BM$, 3F-$PC_{61}BM$ and 5F-$PC_{61}BM$. The data are shown in the ESI.† Fig. S1(a)† shows the cell architecture. Fig. S1(b)† shows the measured current density–effective voltage curves, and the results are summarized in Table S1.† The electron mobilities of $PC_{61}BM$, 3F-$PC_{61}BM$ and 5F-$PC_{61}BM$ were estimated to be 4.16×10^{-4} cm^2 V^{-1} s^{-1}, 5.61×10^{-4} cm^2 V^{-1} s^{-1} and 2.69×10^{-4} cm^2 V^{-1} s^{-1}, respectively. The slight decrease in the electron mobility of 5F-$PC_{61}BM$ molecules may have resulted from the poor molecular packing of the bulky pentafluoropropyl groups. However, all the mobilities of fluorinated $PC_{61}BM$ were still of the same order of 10^{-4} cm^2 V^{-1} s^{-1} as that of $PC_{61}BM$. This indicates that fluorinated $PC_{61}BM$ has a comparable ability to transport electrons.

Besides the carrier mobility of fluorinated $PC_{61}BM$, we also needed to ensure that the energy levels of fluorinated $PC_{61}BM$ were appropriate for the BHJ device. Combined cyclic voltammetry (CV) and ultraviolet-visible absorption spectroscopy (UV-vis) measurements were carried out to determine the lowest unoccupied molecular orbital (LUMO) and highest occupied molecular orbital (HOMO) of fluorinated $PC_{61}BM$, as shown in Fig. S2(a) and S2(b).† The calculated energy levels are listed in Table S2.† The LUMO levels of $PC_{61}BM$, 3F-$PC_{61}BM$ and 5F-$PC_{61}BM$ were determined by the following equation: $E_{LUMO} = -e[E_{red}^{onset} + 4.6]$, where E_{red}^{onset} is the reduction potential for the sample. The HOMO levels were estimated by subtracting the LUMO levels from the values of the band gap, which were derived from the UV-vis absorption spectra. Both the HOMO and the LUMO levels of 3F-$PC_{61}BM$ and 5F-$PC_{61}BM$ are lower than the energy levels of $PC_{61}BM$ by 0.2 eV. This is due to the presence of strongly electron-withdrawing fluoroalkyl groups in fluorinated $PC_{61}BM$, which causes fluorinated $PC_{61}BM$ to become more electron-deficient. Thus, fluorinated $PC_{61}BM$ exhibits a negative shift in energy levels from those of pristine $PC_{61}BM$. The band diagram of our BHJ device is shown in Fig. S2(c).† The built-in potential of the BHJ absorption layer is still suitable for the separation of excitons. There is also no energy barrier in the BHJ band diagram to block the transport of electrons or holes from the light-absorbing layer to the counter electrodes. In summary, the fluoroalkyl group in fluorinated $PC_{61}BM$ can modify fluorinated $PC_{61}BM$ so as to have higher solubility than $PC_{61}BM$ without sacrificing its optical and electrical properties.

After the characterization of the basic properties of the materials, we blended different amounts of either 3F-$PC_{61}BM$ or 5F-$PC_{61}BM$ (based on the weight of perovskite) into the perovskite precursor to prepare the BHJ precursor solutions. Fig. 1(c)–(e) are photos of our BHJ precursor solutions without filtration. Fig. 1(c) compares the difference in the appearance of the solution between the pristine perovskite precursor solution and the BHJ precursor solution containing 0.1 wt% $PC_{61}BM$. Owing to the poor solubility of $PC_{61}BM$ in DMF, there were many insoluble aggregates in the BHJ precursor solution, which made the solution turbid. However, the BHJ precursor solutions blended with 3F-$PC_{61}BM$ and 5F-$PC_{61}BM$, as shown in Fig. 1(d) and (e), all remained transparent even at high concentrations of 0.5 wt% 3F-$PC_{61}BM$ and 5F-$PC_{61}BM$. By filtration, almost all the insoluble aggregates in the 0.1 wt% $PC_{61}BM$: perovskite BHJ precursor solution were removed and its color was similar to that of the pristine perovskite solution, as shown in Fig. 1(f). On the other hand, there was no color change after filtration for the BHJ precursor solutions containing 3F-$PC_{61}BM$ and 5F-$PC_{61}BM$, as shown in Fig. 1(g) and (h). Thus, 3F-$PC_{61}BM$ and 5F-$PC_{61}BM$ could be homogeneously dispersed in the perovskite precursor solution and were suitable for fabricating BHJ perovskite solar cells.

To determine the optimized concentrations of 3F-$PC_{61}BM$ and 5F-$PC_{61}BM$ in the perovskite precursor solution for the fabrication of devices, we varied their concentrations from 0.05 wt% to 0.5 wt%. The measured current density–voltage (J–V) curves of fluorinated $PC_{61}BM$: perovskite BHJ devices are shown in Fig. S3,† and their corresponding photovoltaic parameters are summarized in Tables S3 and S4,† respectively. The pristine device exhibited a PCE of 14.12% with an

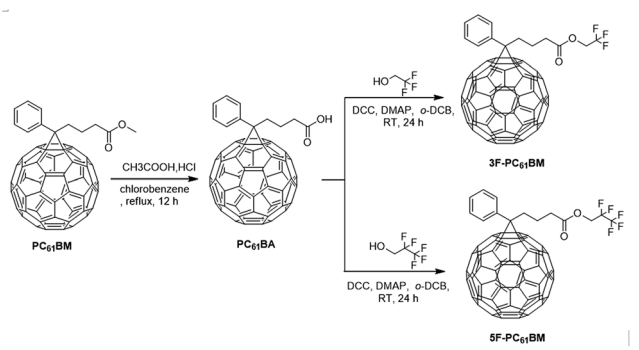

Scheme 1 Chemical reactions in syntheses of 3F-$PC_{61}BM$ and 5F-$PC_{61}BM$.

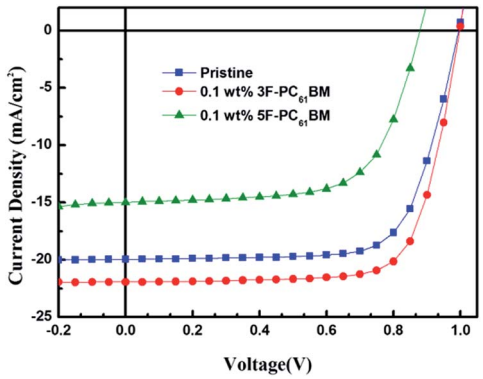

Fig. 2 *J–V* curves of pristine device and BHJ devices blended with 0.1 wt% 3F-$PC_{61}BM$ and 0.1 wt% 5F-$PC_{61}BM$.

open-circuit voltage (V_{oc}) of 1.01 V, a short-circuit current density (J_{sc}) of 19.96 mA cm^{-2} and a fill factor (FF) of 71.10%. Upon the incorporation of 0.05 wt% 3F-$PC_{61}BM$, there was almost no difference in performance between the pristine device and the BHJ device. Therefore, we further increased the concentration of 3F-$PC_{61}BM$ to 0.1 wt%. The performance was significantly improved and included a PCE of 16.17% with a V_{oc} of 1.00 V, a J_{sc} of 21.78 mA cm^{-2}, and an FF of 73.34%. However, as the concentration of 3F-$PC_{61}BM$ in the BHJ film was further increased to greater than 0.1 wt%, the performance of BHJ devices started to decrease, as shown by the PCEs of 13.58% and 12.67% when blending amounts of 0.3 wt% and 0.5 wt% of 3F-$PC_{61}BM$ were used, respectively. On the other hand, for 5F-$PC_{61}BM$: perovskite BHJ devices, no matter what the concentration of 5F-$PC_{61}BM$ was in the BHJ films, the performance of BHJ devices was always worse than that of the pristine device. In order to study how the number of fluorine atoms affected the performance of BHJ devices, we fixed the concentration of fluorinated $PC_{61}BM$ in the perovskite layer at 0.1 wt% and compared the device performance with that of the pristine device. We fabricated 15 devices for each kind of perovskite composition, and their photovoltaic performance was evaluated and the standard deviations were calculated. The *J–V* curves and performance of these three types of devices are summarized in Fig. 2 and Table 1. The data show that the increase in the average PCE for the device containing 0.1 wt% 3F-$PC_{61}BM$ was statistically significant in comparison with that of the pristine device. At the same concentration of 0.1 wt%, 3F-$PC_{61}BM$ molecules effectively increased the J_{sc} and PCE from 19.96 mA cm^{-2} and 14.12% for the pristine device to 21.78 mA cm^{-2} and 16.17%, respectively, whereas 5F-$PC_{61}BM$ molecules caused dramatic decreases in V_{oc} to 0.87 V, J_{sc} to 14.99 mA cm^{-2}, FF to 65.71% and PCE to 8.65%. It can be concluded that the performance of the BHJ devices was closely related to the length of the fluoroalkyl chain in fluorinated $PC_{61}BM$. We therefore investigated how the fluorinated $PC_{61}BM$ affected the properties of BHJ films *via* optical and morphological studies.

Table 1 Device performance of BHJ perovskite solar cells containing different amounts of fluorinated $PC_{61}BM$

Device	V_{oc} (V)	J_{sc} (mA cm^{-2})	FF (%)	PCE (%)
0 wt%	1.01	19.96	71.10	14.12 (13.36 ± 0.64)
0.1 wt% 3F-$PC_{61}BM$	1.00	21.78	73.34	16.17 (14.93 ± 0.71)
0.1 wt% 5F-$PC_{61}BM$	0.87	14.99	65.71	8.65 (7.66 ± 1.02)

We first analyzed the difference in carrier extraction efficiency between the pristine perovskite film and 0.1 wt% fluorinated $PC_{61}BM$: perovskite BHJ films using photoluminescence (PL) spectroscopy, as illustrated in Fig. 3(a). Significant quenching of the PL intensity was observed for the BHJ perovskite films. This illustrates that the incorporation of fluorinated $PC_{61}BM$ into the light-absorbing layer can increase the size of the heterojunction between perovskite and fluorinated $PC_{61}BM$. The extraction of photogenerated excitons is more effective, which reduces the possibility of recombination. Therefore, time-resolved photoluminescence (TRPL) measurements were used to study the charge dissociation ability in the pristine perovskite film and 0.1 wt% fluorinated $PC_{61}BM$: perovskite BHJ films, as shown in Fig. 3(b). The related parameters are summarized in Table 2. All the exponential decay profiles are fitted by the bi-exponential model ($I(t) = A_1e_1^{-t/\tau} + A_2e_2^{-t/\tau}$), which includes a charge transfer mechanism (fraction A_1, time for charge transfer τ_1) and a radiative decay mechanism (fraction A_2, time for radiative decay τ_2).[32] Here, charge transfer

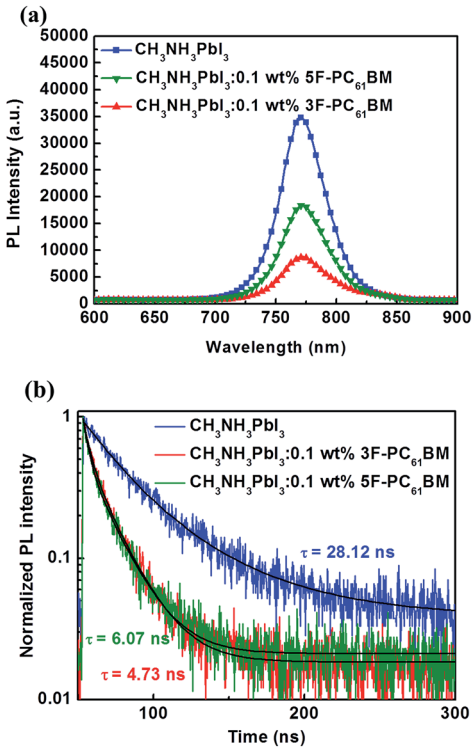

Fig. 3 (a) Photoluminescence spectra of pristine perovskite film, 0.1 wt% 3F-$PC_{61}BM$: perovskite and 0.1 wt% 5F-$PC_{61}BM$: perovskite BHJ films. (b) Time-resolved photoluminescence characterization of pristine perovskite film, 0.1 wt% 3F-$PC_{61}BM$: perovskite and 0.1 wt% 5F-$PC_{61}BM$: perovskite BHJ films.

Table 2 Fitting results of time-resolved photoluminescence characterization

Sample	τ_1 (ns)	Fraction (%)	τ_2 (ns)	Fraction (%)	$\tau_{Average}$ (ns)
$CH_3NH_3PbI_3$	24.16	88	56.69	12	28.12
$CH_3NH_3PbI_3$:0.1 wt% 3F-$PC_{61}BM$	4.72	99	18.23	1[a]	4.73
$CH_3NH_3PbI_3$:0.1 wt% 5F-$PC_{61}BM$	5.93	99	20.65	1[a]	6.07

[a] In these cases, the radiative decay contribution is certainly not larger than the experimental error.

is the dominant mechanism that affects the decay of intensity. We thus put emphasis on the time required for charge transfer and the charge transfer fraction. For the pristine perovskite film, the time required for charge transfer was 24.16 ns and the charge transfer fraction was 88%. Upon blending 0.1 wt% 3F-$PC_{61}BM$ into the perovskite film, the time required for charge transfer decreased from 24.16 ns to 4.72 ns, and the charge transfer fraction increased from 88% to 99%. This means that once excitons were generated by incident light in the perovskite material, they could be very efficiently separated. In addition, blending 0.1 wt% 5F-$PC_{61}BM$ into the perovskite film also decreased the time required for charge transfer to 5.93 ns and increased the charge transfer fraction to 99%. Although the BHJ film blended with 0.1 wt% 5F-$PC_{61}BM$ had a better ability to transfer carriers in comparison with the pristine perovskite film, all the performance parameters of the 0.1 wt% 5F-$PC_{61}BM$: perovskite BHJ device were worse than those of the pristine device. This motivated us to carry out an in-depth analysis of the morphology of the BHJ perovskite films so that we could understand the effect of fluorinated $PC_{61}BM$ on the performance of BHJ devices.

SEM was employed to analyze the surface morphology of the BHJ perovskite films. Fig. 4 shows top-view SEM images of the pristine perovskite film and 0.1 wt% fluorinated $PC_{61}BM$: perovskite BHJ films on the substrate of ITO/PEDOT:PSS. SEM images of BHJ perovskite films containing different concentrations of fluorinated $PC_{61}BM$ are shown in Fig. S4.† The pristine perovskite film consisted of many small grains that were distributed randomly, which resulted in a relatively rough surface (Fig. 4(a)). For the 0.1 wt% 3F-$PC_{61}BM$: perovskite BHJ film, its surface became smoother than that of the pristine perovskite film. 3F-$PC_{61}BM$ was homogeneously dispersed in the grain boundaries of perovskite, passivated the defects and formed a smooth film (Fig. 4(b)), which improved the contact between the perovskite film and the electron transport layer.

Moreover, the incorporated 3F-$PC_{61}BM$ could effectively separate excitons and extract charges from perovskite, whereby the J_{sc} and PCE were increased and outperformed those of the pristine device. When we increased the concentration of 3F-$PC_{61}BM$ from 0.1 wt% to 0.5 wt%, there were some aggregated clusters on the surface of the film Fig. S4(a) and (b).† This was due to the low surface energy of 3F-$PC_{61}BM$ molecules, which undergo phase separation and form aggregates and voids at

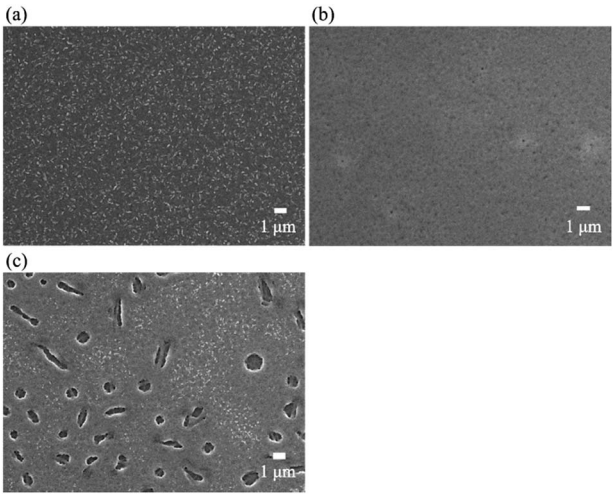

Fig. 4 SEM images of (a) pristine perovskite film; (b) 0.1 wt% 3F-$PC_{61}BM$: perovskite BHJ film; and (c) 0.1 wt% 5F-$PC_{61}BM$: perovskite BHJ film.

higher concentrations in BHJ films. Thus, the PCE of the BHJ device decreased from 16.17% to 12.67% at a concentration of 0.5 wt% 3F-$PC_{61}BM$ Table S3.† On the other hand, for the BHJ perovskite film containing 0.1 wt% 5F-$PC_{61}BM$, many large holes with a diameter of greater than one micrometer were observed in the film, as shown in Fig. 4(c). The low surface energy of 5F-$PC_{61}BM$ is not compatible with perovskite, which resulted in self-aggregation that obstructed the formation of a continuous film. The presence of holes in the film led to direct contact between the electron transport layer and the hole transport layer, which dramatically decreased the performance of BHJ devices. Therefore, the device exhibited a poor PCE of only 8.65%. A further increase in the amount of 5F-$PC_{61}BM$ led to the over-coalescence of perovskite grains with large voids and even strip like grains, as shown in Fig. S4(c) and (d).† The PCE of the BHJ device dramatically declined to 4.30% at a concentration of 0.5 wt% 5F-$PC_{61}BM$ Table S4.†

The morphology of BHJ films was further studied by AFM to visualize the roughness and depth profile of the as-deposited films. Fig. 5 shows the AFM topography and depth information of the pristine perovskite film and 0.1 wt% fluorinated $PC_{61}BM$: perovskite BHJ films. The AFM topographies of the 0.3 wt% and 0.5 wt% fluorinated $PC_{61}BM$: perovskite BHJ films are shown in Fig. S5 and S6.† The pristine perovskite film with small disordered grains exhibited a root mean square roughness (RMS) of 16.90 nm (Fig. 5(a)). The addition of 0.1 wt% 3F-$PC_{61}BM$ to the perovskite film (Fig. 5(b)) caused the RMS to be significantly reduced to 8.33 nm. We speculate that 3F-$PC_{61}BM$ filled the defects of perovskite and made the film smoother. The causes of the increased smoothness were investigated by GISAXS and GIWAXS. The results will be discussed in detail in the next section. The improved morphology of the 0.1 wt% 3F-$PC_{61}BM$: perovskite film increased the PCE of the device from 14.12% to 16.17%. On the other hand, the BHJ perovskite film containing 0.1 wt% 5F-$PC_{61}BM$ had an RMS of 64.90 nm (Fig. 5(c)). The holes in the film were deep enough for direct

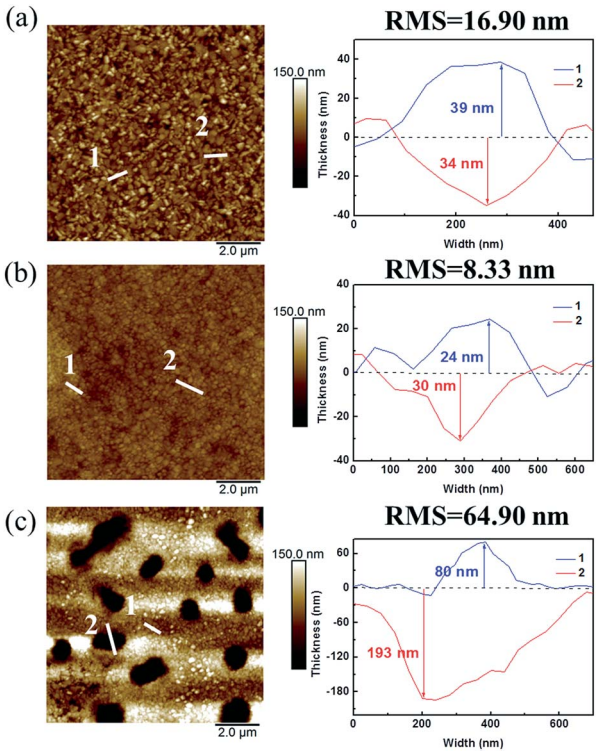

Fig. 5 AFM surface height images and depth information of (a) pristine perovskite film; (b) 0.1 wt% 3F-$PC_{61}BM$: perovskite BHJ film; and (c) 0.1 wt% 5F-$PC_{61}BM$: perovskite BHJ film.

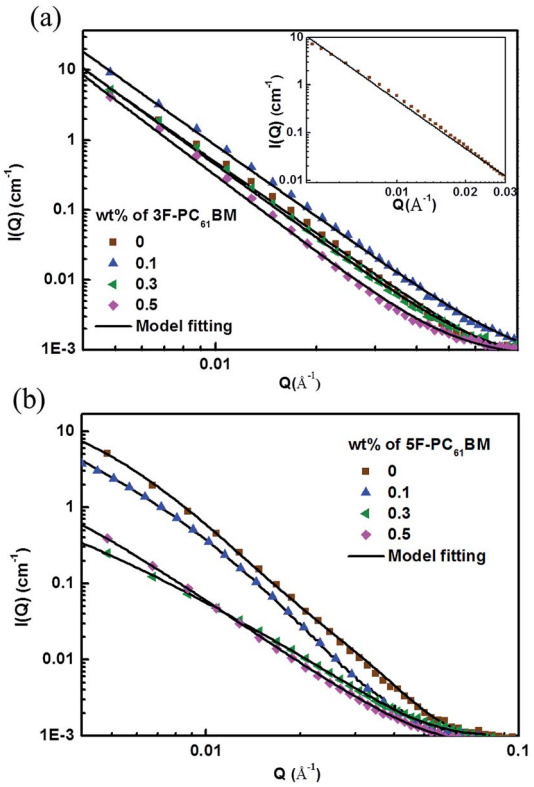

Fig. 6 (a) GISAXS profiles of BHJ perovskite films made from different concentrations of 3F-$PC_{61}BM$. The solid lines were calculated using a power-law model, and the inset figure is a magnification of the profile of the pristine film in the central Q range to show the mismatch between the raw data and the model fitting. (b) GISAXS profiles of BHJ perovskite films made from different concentrations of 5F-$PC_{61}BM$. The solid lines were calculated using a fractal polysphere model.

contact between the electron transport layer and the hole transport layer, so that the 0.1 wt% 5F-$PC_{61}BM$: perovskite BHJ device exhibited a poor PCE of 8.65%. As the concentration of 3F-$PC_{61}BM$ was increased to 0.3 wt% or 0.5 wt%, although the RMS of the 3F-$PC_{61}BM$: perovskite BHJ films was still lower than that of the pristine perovskite film, aggregated clusters on the surface of the BHJ perovskite films gradually grew, as shown in Fig. S5.† The aggregated clusters resulted in poor contact between the BHJ film and the electron transport layer. Thus, the device performance decreased with an increase in the concentration of 3F-$PC_{61}BM$. The surface roughness of 5F-$PC_{61}BM$: perovskite BHJ films increased further when the concentration of 5F-$PC_{61}BM$ was increased to 0.3 wt% and 0.5 wt% Fig. S6.† The depths of voids could be as great as 239 and 260 nm for the 0.3 wt% and 0.5 wt% 5F-$PC_{61}BM$: perovskite BHJ films, respectively. Thus, the PCE of the 0.3 wt% and 0.5 wt% 5F-$PC_{61}BM$: perovskite BHJ devices decreased to 5.82% and 4.30%, respectively, from the value of 8.65% of the 0.1 wt% 5F-$PC_{61}BM$: perovskite BHJ device.

The study of surface morphology by SEM and AFM is limited to a very local small area. We employed simultaneous synchrotron GISAXS/GIWAXS measurements to investigate the detailed bulk morphology of the fluorinated $PC_{61}BM$: perovskite BHJ films. Fig. 6(a) shows the GISAXS profiles of the pristine perovskite film and the BHJ films containing 0.1, 0.3 and 0.5 wt% 3F-$PC_{61}BM$. The GISAXS profiles of all the BHJ films display power-law scattering behavior ($I(Q) \propto Q - \alpha$) in the Q region of 0.005–0.05 Å^{-1}. Here, the exponent α is related to the fractal dimension D, where $D = 6 - \alpha$.[33] The D values of the pristine perovskite film and the 3F-$PC_{61}BM$ BHJ films are summarized in Table 3. The D values of the BHJ films were between 2 and 3, which reveals surface fractal characteristics. The surface fractal indicates that the films had a two-dimensional (2D) self-similar morphology on different scales from nanometers to micrometers. It implies that the internal structures of the films comprised densely packed perovskite grains. Note that the D values decreased as the amount of 3F-$PC_{61}BM$ increased, which means that the addition of 3F-$PC_{61}BM$ molecules can induce the packing of perovskite grains to form a dense film. However, an excess amount of 3F-$PC_{61}BM$ (greater than 0.1 wt%) induced phase separation, and self-aggregated clusters and voids thus formed on the surface and in the bulk of the BHJ film, as observed in the SEM images (Fig. S4†) and AFM images (Fig. S5†), which resulted in poor contact between the BHJ film and the electron transport layer. As a result, the device performance decreased. In contrast to the BHJ films, the GISAXS profile of the pristine perovskite film displays similar power-law scattering characteristics except for a weak shoulder in the central Q region of 0.009–0.03 Å^{-1} (Fig. 6(a) inset). Thus, the pristine perovskite film mainly had the characteristics of a porous structure. It can be concluded that the incorporation of 3F-$PC_{61}BM$ molecules significantly

Table 3 Structural parameters determined by power-law model fitting for the BHJ perovskite films blended with different concentrations of 3F-$PC_{61}BM$ using GISAXS spectroscopy

wt% of 3F-$PC_{61}BM$ in active layer	Fractal type	D
0	Pore	2.95[a]
0.1	Surface	2.63
0.3	Surface	2.53
0.5	Surface	2.38

[a] The power-law cannot fit the GISAXS profile of the 0 wt% perovskite film well.

influenced the formation behavior and structure of the perovskite film, including the bulk and surface morphologies. A schematic illustration of the formation of the BHJ film containing 3F-$PC_{61}BM$ is shown in Fig. 7(a). At an appropriate amount (0.1 wt%), 3F-$PC_{61}BM$ could disperse well in the perovskite precursor solution and help the nucleation and growth of perovskite grains into a densely packed film.

The GISAXS profiles of the BHJ films containing 0.1, 0.3 and 0.5 wt% 5F-$PC_{61}BM$ are shown in Fig. 6(b). All the GISAXS profiles display power-law scattering behavior in the low Q range (0.005–0.02 $Å^{-1}$). The values of the fractal dimension Q were between 3 and 4, which indicates that all the 5F-$PC_{61}BM$: perovskite BHJ films had mass fractal characteristics. The mass fractal morphology comprised a fractal network structure formed by the aggregation of primary particles. Therefore, in order to fit the GISAXS profiles well over the whole Q range, the fitting model needs to contain the form factor $P(Q)$ of the primary particles and the structure factor $S(Q)$ of the mass fractal network. The model fitting profile can be expressed as the following equation:

$$I(Q) = P(Q)S(Q) \quad (1)$$

From a previous report, we know that the primary particles in a perovskite film with mass fractal morphology have a porous structure.[33] The calculation of $P(Q)$ considers the mean radius R of primary pores with a standard deviation of the size distribution (polydispersity) of p. $S(Q)$ describes the interaction between primary pores in the mass fractal network system, which is expressed below:

$$S(Q) = 1 + \frac{\sin\left[(D-1) + \tan^{-1}(Q\xi)\right]}{(QR)^D} \frac{D\Gamma(D-1)}{\left[1 + 1\Big/(Q\xi)^2\right]^{(D-1)/2}} \quad (2)$$

where ξ is the correlation length of the fractal pore network system, which denotes the distance between aggregates of primary pores, D_p is the mass fractal dimension, and $\Gamma(D_p - 1)$ is the gamma function of the variable $(D_p - 1)$. The fitted parameters of the fractal pore network in the perovskite grains or between the grain boundaries are listed in Table 4.

The fitting results show that the polydisperse primary pores in the pristine perovskite film had a mean radius of 4.9 nm with a correlation length of ~24 nm. Upon the addition of 0.1 wt% of 5F-$PC_{61}BM$ to the film, the pore size decreased to 3.7 nm with a slight increase in the correlation length to ~25 nm. The radius of the primary pores further decreased to ~2.8 nm and the correlation length of the fractal domains increased to ~40 nm when the amount of 5F-$PC_{61}BM$ was increased to 0.3 or 0.5 wt%. The changes in the pore size and correlation length with different amounts of 5F-$PC_{61}BM$ can be used to explain the changes in morphology observed in the SEM and AFM studies. We speculate that 5F-$PC_{61}BM$ molecules in the perovskite could substantially aggregate, even though their amount was low. A schematic illustration of the formation of a BHJ film containing 5F-$PC_{61}BM$ is shown in Fig. 7(b). As the amount of 5F-$PC_{61}BM$ in the film increased, extensive aggregation behavior led to heterogeneous nucleation and the growth of perovskite crystallites followed by the over-coalescence of grains with large voids and even strip-like grains.

Fig. 8 shows the 2D GIWAXS patterns of the pristine perovskite film and the BHJ films containing 0.1 wt% fluorinated $PC_{61}BM$. All the films displayed the preferred orientation of perovskite crystallites with the diffraction spot of the (110) plane in the out-of-plane direction (normal to the film or substrate surface). The calculated sizes of the perovskite crystals were all about 40 nm. Among these, the 3F-$PC_{61}BM$: perovskite BHJ films exhibited the highest diffraction intensity due to the (110) plane. The homogeneous dispersion of 3F-$PC_{61}BM$ in the grain boundaries could restrict the lateral growth of perovskite grains, which would promote the dense packing of perovskite grains and growth in the out-of-plane direction. The improvement in the crystallinity of perovskite in the out-of-plane direction is beneficial for charge transportation in perovskite solar cells. In contrast, it is difficult for the substantial

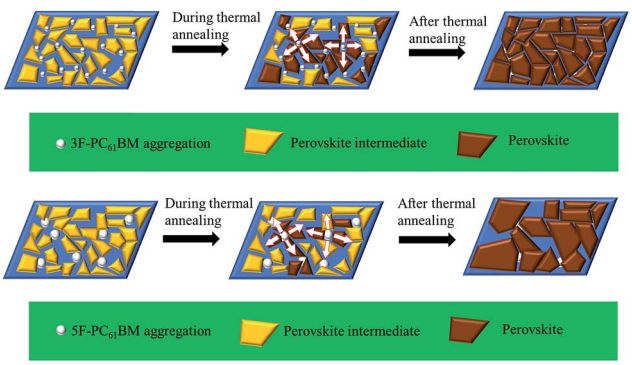

Fig. 7 Schematic illustrations of the formation mechanism of BHJ films containing 3F-$PC_{61}BM$ (up) and 5F-$PC_{61}BM$ (down).

Table 4 Structural parameters determined by fractal polysphere model fitting for the BHJ perovskite films blended with different concentrations of 5F-$PC_{61}BM$ using GISAXS spectroscopy

wt% of 5F-$PC_{61}BM$ in active layer	Fractal type	R (nm)	D_p	p	ζ (nm)
0	Pore	4.9	2.95	0.4	24
0.1	Pore	3.7	2.71	0.6	25
0.3	Pore	2.6	2.18	0.5	40
0.5	Pore	2.8	2.55	0.4	41

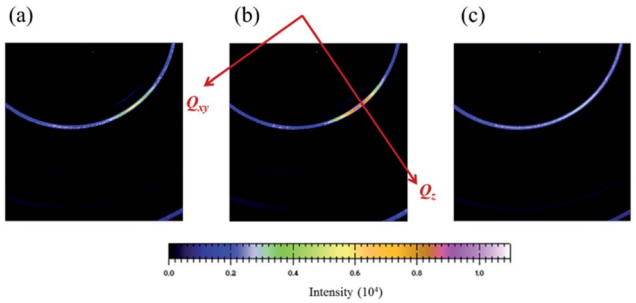

Fig. 8 Two dimensional (2D) GIWAXS patterns of (a) pristine $CH_3NH_3PbI_3$, (b) 0.1 wt% 3F-PC_{61}BM: $CH_3NH_3PbI_3$ and (c) 0.1 wt% 5F-PC_{61}BM: $CH_3NH_3PbI_3$ BHJ films. The Q_z and Q_{xy} directions are the out-of-plane and in-plane directions, respectively.

aggregates of 5F-PC_{61}BM molecules to be homogeneously dispersed in the perovskite grain boundaries. The lateral growth of perovskite grains is not restricted in this case. Therefore, the 5F-PC_{61}BM: perovskite BHJ films exhibited the lowest diffraction intensity due to the (110) plane in the out-of-plane direction among all the films.

Finally, Fig. 9(a) compares the stability of the pristine device and 0.1 wt% 3F-PC_{61}BM: perovskite BHJ device. These devices were stored in a nitrogen-filled glove box without encapsulation. Then, they were taken out of the glove box periodically, and the device performance was measured in ambient conditions (25 °C/50% relative humidity). The PCE of the pristine perovskite solar cell declined to 80% of the original performance after storage for only 240 hours. However, the PCE of the 0.1 wt% 3F-PC_{61}BM: perovskite BHJ device maintained 80% of the original efficiency after 550 hours. We also performed measurements of the water contact angle on the pristine device and 0.1 wt% 3F-PC_{61}BM: perovskite BHJ device in the area without the electrode, as shown in Fig. 9(b). Initially, these two devices had similar water contact angles of about 92°. After 5 min, the water contact angle of the 0.1 wt% 3F-PC_{61}BM: perovskite BHJ device became 57.42°, which was higher than that of the pristine device (36.68°). This difference in the water contact angle was due to the difference in the film morphology. The BHJ film containing 0.1 wt% 3F-PC_{61}BM was flat with fewer pinholes, which can prevent the invasion of moisture into perovskite grain boundaries. The results indicate that the incorporation of 3F-PC_{61}BM can indeed improve the stability of BHJ perovskite solar cells.

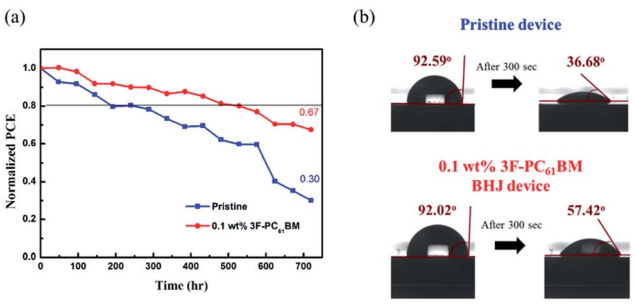

Fig. 9 (a) Stability measurements of pristine and 0.1 wt% 3F-PC_{61}BM: perovskite BHJ solar cells. (b) Contact angle measurements for pristine perovskite device and 0.1 wt% 3F-PC_{61}BM: perovskite BHJ device conducted at 0 s and 300 s.

Conclusions

We successfully incorporated fluorinated PC_{61}BM to fabricate high-performance and stable BHJ perovskite solar cells by a single-solvent one-step solution process. The length of the fluoroalkyl chain in the fluorinated PC_{61}BM derivatives affected their self-aggregation behavior in the BHJ perovskite films. We showed that 0.1 wt% of 3F-PC_{61}BM can be homogeneously dispersed in a BHJ perovskite film and induce the formation of densely packed perovskite grains. Thus, a flat BHJ perovskite film was formed. With respect to the performance of the devices, the J_{sc} and PCE increased from 19.96 mA cm^{-2} and 14.12% for the pristine device to 21.78 mA cm^{-2} and 16.17% for the 0.1 wt% 3F-PC_{61}BM: perovskite BHJ device, respectively. On the other hand, the self-aggregation of 5F-PC_{61}BM molecules occurred more easily in the BHJ perovskite films than that of 3F-PC_{61}BM molecules. This resulted in a large amount of heterogeneous nucleation sites in the BHJ perovskite film for the formation of excessive aggregates of perovskite grains with a discontinuous rough film morphology. The voids in the films would cause direct contact between the electron transport layer and the hole transport layer, which would lead to poor device performance. Thus, the addition of 5F-PC_{61}BM decreased the PCE to less than that of the pristine device, regardless of its amount. We also showed that the dense flat surface morphology of the 0.1 wt% 3F-PC_{61}BM: perovskite BHJ film can effectively suppress the permeation of moisture in ambient conditions. A BHJ device maintained 80% of its initial PCE over 550 hours, whereas that of the pristine device declined to less than 80% of the original value after storage for 240 hours. Our work provides useful knowledge that by the selection of an appropriate fluoroalkyl chain and concentration of fluorinated PC_{61}BM we can easily fabricate high-performance and high-stability BHJ devices *via* a simple single-solvent one-step solution process.

Conflicts of interest

There are no conflicts to declare.

Acknowledgements

The authors highly appreciated the financial support obtained from the Ministry of Science and Technology of Taiwan in this research (MOST 105-3113-E-002-010 and MOST 106-3113-E-002-008-CC2).

References

1 H. J. Snaith and M. Grätzel, *Adv. Mater.*, 2007, **19**, 3643–3647.
2 S. D. Stranks, G. E. Eperon, G. Grancini, C. Menelaou, M. J. P. Alcocer, T. Leijtens, L. M. Herz, A. Petrozza and H. J. Snaith, *Science*, 2013, **342**, 341–344.

3 L. M. Pazos-Outón, M. Szumilo, R. Lamboll, J. M. Richter, M. Crespo-Quesada, M. Abdi-Jalebi, H. J. Beeson, M. Vrućinić, M. Alsari, H. J. Snaith, B. Ehrler, R. H. Friend and F. Deschler, *Science*, 2016, **351**, 1430–1433.
4 Q. Dong, Y. Fang, Y. Shao, P. Mulligan, J. Qiu, L. Cao and J. Huang, *Science*, 2015, **347**, 967–970.
5 G. Xing, N. Mathews, S. Sun, S. S. Lim, Y. M. Lam, M. Grätzel, S. Mhaisalkar and T. C. Sum, *Science*, 2013, **342**, 344–347.
6 D. Shi, V. Adinolfi, R. Comin, M. Yuan, E. Alarousu, A. Buin, Y. Chen, S. Hoogland, A. Rothenberger, K. Katsiev, Y. Losovyj, X. Zhang, P. A. Dowben, O. F. Mohammed, E. H. Sargent and O. M. Bakr, *Science*, 2015, **347**, 519–522.
7 G. E. Eperon, S. D. Stranks, C. Menelaou, M. B. Johnston, L. M. Herz and H. J. Snaith, *Energy Environ. Sci.*, 2014, **7**, 982–988.
8 J. H. Noh, S. H. Im, J. H. Heo, T. N. Mandal and S. I. Seok, *Nano Lett.*, 2013, **13**, 1764–1769.
9 S. De Wolf, J. Holovsky, S. J. Moon, P. Loper, B. Niesen, M. Ledinsky, F. J. Haug, J. H. Yum and C. Ballif, *J. Phys. Chem. Lett.*, 2014, **5**, 1035–1039.
10 Q. Lin, A. Armin, R. C. R. Nagiri, P. L. Burn and P. Meredith, *Nat. Photonics*, 2014, **9**, 106–112.
11 NREL, http://www.nrel.gov/ncpv/, updated 04/14/2017.
12 A. Kojima, K. Teshima, Y. Shirai and T. Miyasaka, *J. Am. Chem. Soc.*, 2009, **131**, 6050–6051.
13 W. S. Yang, J. H. Noh, N. J. Jeon, Y. C. Kim, S. Ryu, J. Seo and S. I. Seok, *Science*, 2015, **348**, 1234–1237.
14 H. S. Kim, C. R. Lee, J. H. Im, K. B. Lee, T. Moehl, A. Marchioro, S. J. Moon, R. Humphry-Baker, J. H. Yum, J. E. Moser, M. Gratzel and N. G. Park, *Sci. Rep.*, 2012, **2**, 591–597.
15 M. M. Lee, J. Teuscher, T. Miyasaka, T. N. Murakami and H. J. Snaith, *Science*, 2012, **338**, 643–647.
16 J. M. Ball, M. M. Lee, A. Hey and H. J. Snaith, *Energy Environ. Sci.*, 2013, **6**, 1739–1743.
17 T. Leijtens, G. E. Eperon, S. Pathak, A. Abate, M. M. Lee and H. J. Snaith, *Nat. Commun.*, 2013, **4**, 2885–2892.
18 Q. Chen, H. Zhou, Z. Hong, S. Luo, H. S. Duan, H. H. Wang, Y. Liu, G. Li and Y. Yang, *J. Am. Chem. Soc.*, 2014, **136**, 622–625.
19 K. Wojciechowski, M. Saliba, T. Leijtens, A. Abate and H. J. Snaith, *Energy Environ. Sci.*, 2014, **7**, 1142–1147.
20 H. Zhou, Q. Chen, G. Li, S. Luo, T. B. Song, H. S. Duan, Z. Hong, J. You, Y. Liu and Y. Yang, *Science*, 2014, **345**, 542–546.
21 J. Y. Jeng, Y. F. Chiang, M. H. Lee, S. R. Peng, T. F. Guo, P. Chen and T. C. Wen, *Adv. Mater.*, 2013, **25**, 3727–3732.
22 C. Y. Chang, C. Y. Chu, Y. C. Huang, C. W. Huang, S. Y. Chang, C. A. Chen, C. Y. Chao and W. F. Su, *ACS Appl. Mater. Interfaces*, 2015, **7**, 4955–4961.
23 J. Xu, A. Buin, A. H. Ip, W. Li, O. Voznyy, R. Comin, M. Yuan, S. Jeon, Z. Ning, J. J. McDowell, P. Kanjanaboos, J. P. Sun, X. Lan, L. N. Quan, D. H. Kim, I. G. Hill, P. Maksymovych and E. H. Sargent, *Nat. Commun.*, 2015, **6**, 7081–7088.
24 C. H. Chiang and C. G. Wu, *Nat. Photonics*, 2016, **10**, 196–200.
25 M. Li, Y. H. Chao, T. Kang, Z. K. Wang, Y. G. Yang, S. L. Feng, Y. Hu, X. Y. Gao, L. S. Liao and C. S. Hsu, *J. Mater. Chem. A*, 2016, **4**, 15088–15094.
26 X. Liu, F. Lin, C. C. Chueh, Q. Chen, T. Zhao, P. W. Liang, Z. Zhu, Y. Sun and A. K. Y. Jen, *Nano Energy*, 2016, **30**, 417–425.
27 K. Wang, C. Liu, P. Du, J. Zheng and X. Gong, *Energy Environ. Sci.*, 2015, **8**, 1245–1255.
28 C. Liu, K. Wang, P. Du, C. Yi, T. Meng and X. Gong, *Adv. Energy Mater.*, 2015, **5**, 1402024–1402030.
29 M. Xiao, F. Huang, W. Huang, Y. Dkhissi, Y. Zhu, J. Etheridge, A. Gray-Weale, U. Bach, Y. B. Cheng and L. Spiccia, *Angew. Chem., Int. Ed. Engl.*, 2014, **53**, 9898–9903.
30 N. Cho, H. L. Yip, S. K. Hau, K. S. Chen, T. W. Kim, J. A. Davies, D. F. Zeigler and A. K. Y. Jen, *J. Mater. Chem.*, 2011, **21**, 6956–6961.
31 W. Zhang, M. Saliba, D. T. Moore, S. K. Pathak, M. T. Horantner, T. Stergiopoulos, S. D. Stranks, G. E. Eperon, J. A. Alexander-Webber, A. Abate, A. Sadhanala, S. Yao, Y. Chen, R. H. Friend, L. A. Estroff, U. Wiesner and H. J. Snaith, *Nat. Commun.*, 2015, **6**, 6142–6151.
32 P. W. Liang, C. Y. Liao, C. C. Chueh, F. Zuo, S. T. Williams, X. K. Xin, J. Lin and A. K. Jen, *Adv. Mater.*, 2014, **26**, 3748–3754.
33 Y. C. Huang, C. S. Tsao, Y. J. Cho, K. C. Chen, K. M. Chiang, S. Y. Hsiao, C. W. Chen, C. J. Su, U. S. Jeng and H. W. Lin, *Sci. Rep.*, 2015, **5**, 13657–13667.